JOURNAL OF GEOPHYSICAL RESEARCH: PLANETS, VOL. 118, 2570–2581, doi:10.1002/2013JE004469, 2013

Estimates of seismic activity in the Cerberus Fossae region of Mars

J. Taylor,[1] N. A. Teanby,[1] and J. Wookey[1]

Received 2 July 2013; revised 7 October 2013; accepted 13 November 2013; published 23 December 2013.

[1] The 2016 NASA InSight lander is the first planetary mission designed to study the deep interior of Mars. InSight's Seismic Experiment for Interior Structure (SEIS) package will quantify global and regional seismic activity and determine parameters like core properties, mantle composition, and Martian lithospheric thickness. An improved understanding of the location, magnitude, and frequency of potential seismic sources is essential for optimization of instrument design, sampling strategy, and interpretation of mission data. We focus on forecasting seismic activity for the Cerberus Fossae of the Elysium Planitia, chosen for their proximity to the proposed landing site and their recent formation and assuming these are active tectonic grabens. The minimum age we determine for the units around the Fossae, using Context Camera and High Resolution Imaging Science Experiment imagery for crater density surveying, is 10 Ma, placing them in the Late Amazonian. We are able to determine the rate of motion from measurements of observed throw, assuming that the faults remain active. Digital terrain models, made from stereo-image pairs from the High Resolution Stereo Camera (HRSC), are used to determine the maximum throw on four graben systems. Using these measured throws to estimate a length-averaged slip and assuming an inferred slip rate from surface age, we estimate an annual moment release of $1.58^{+2.35}_{-1.03} \times 10^{17}$ Nm. From this we calculate an annual size-frequency distribution of events using the Gütenberg-Richter relationship. We estimate that between 1.5×10^{0} and 1.9×10^{5} events per year will have an amplitude greater than the peak band noise and so will be detectable at the InSight landing site.

Citation: Taylor, J., N. A. Teanby, and J. Wookey (2013), Estimates of seismic activity in the Cerberus Fossae region of Mars, *J. Geophys. Res. Planets*, *118*, 2570–2581, doi:10.1002/2013JE004469.

1. Introduction

[2] Seismology, as a method of probing the deep interior of planets, is vital for our understanding of how these systems developed and evolved. Without it, for example, radial density and composition models remain nonunique and the size and state of planetary cores cannot be accurately determined, making missions such as NASA's InSight lander essential. Mars InSight (Interior Exploration using Seismic Investigations, Geodesy and Heat Transport) is scheduled for launch in March of 2016. It will carry two seismometers in its payload—one very broadband (VBB) and one short period (SP) instrument, along with a heat-flow probe and a radio tracker for observation of orbital parameters. This will allow accurate observation of Martian seismic activity and heat flux for the first time. It is the knowledge of these parameters that has provided such a detailed insight into the structure, composition, and dynamics of our own planet; without them, we would never attain such understanding of the other terrestrial planets [*Lognonné and Mosser*, 1993; *Lognonné*, 2005], nor build a complete picture of the process that governed the formation of the solar system.

[3] The Seismic Experiment for Interior Structure (SEIS) package aboard the InSight lander will record seismic activity on Mars over the mission's forecast 2 year lifespan. The nominal mission science goals depend on the occurrence of detectable seismic events, the number of which is currently poorly constrained. It is therefore imperative that all possible seismic sources be characterized in order to optimize data return from these instruments. In the first instance, characterizing seismic sources will inform the placement of instruments on the surface of Mars in future missions. The instruments should be placed in areas where they are more likely to record events and the source type may also influence the design of the instruments. Potential sources include tectonic activity [*Anderson et al.*, 2001], meteorite impacts [*Teanby and Wookey*, 2011; *Davis*, 1993], and the so-called "atmospheric hum" caused by excitation of normal modes [*Banerdt*, 2010; *Lognonné*, 2009]. Of these, faulting is predicted to be by far the most reliable source of observable seismic energy.

[4] Previous work has focused on producing globally and temporally averaged faulting estimates. *Golombek et al.* [1992] measured the total slip on all major faults, particularly in the Tharsis region, and, assuming a double-couple source, calculated the total seismic moment release. They then distributed this total moment using a moment

[1]Department of Earth Sciences, University of Bristol, Bristol, UK.

Corresponding author: J. Taylor, Department of Earth Sciences, University of Bristol, Wills Memorial Building, Queen's Rd, Clifton, Bristol BS8 1RJ, UK. (jennifer.taylor@bristol.ac.uk)

2169-9097/13/10.1002/2013JE004469

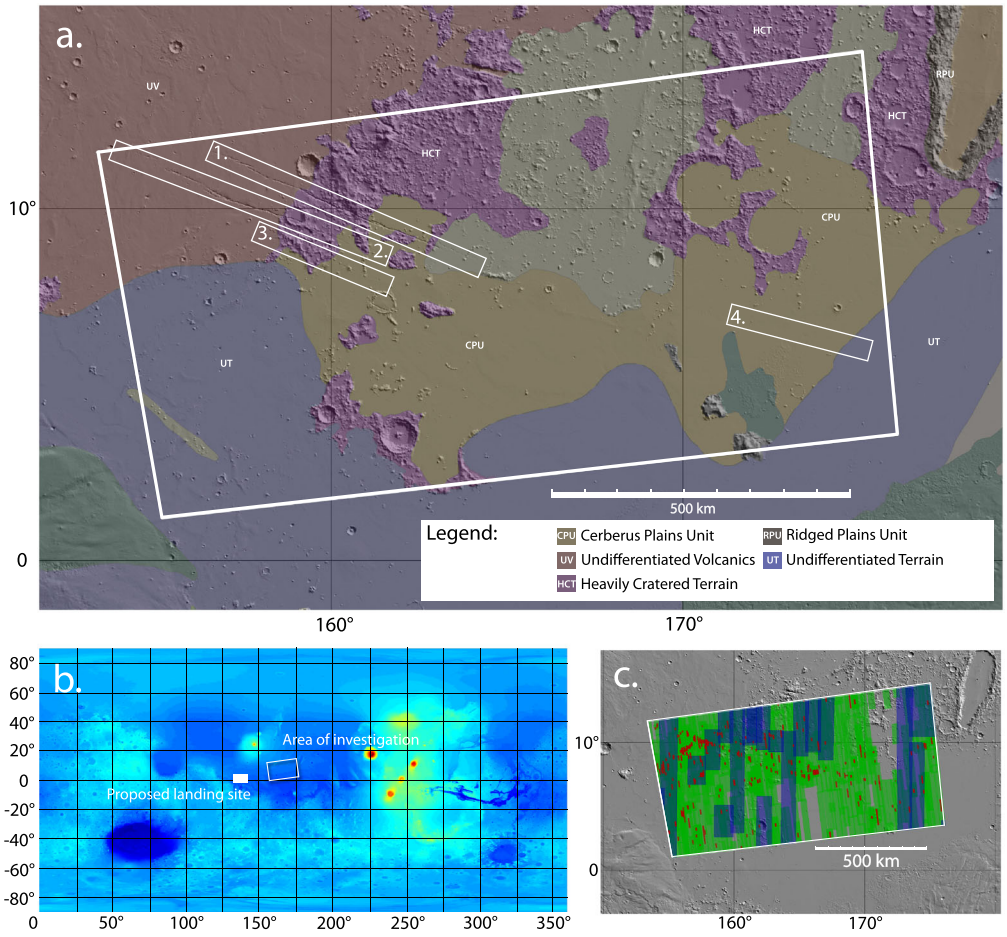

Figure 1. The Cerberus Fossae in their global and geological context. (a) The location of the Cerberus Fossae (graben 1 and 2) and associated minor fault systems (3 and 4) on the Elysium Planitia. Geological map, [*Skinner et al.*, 2006], shows the main geological units of interest and geological unit names from *Plescia* [1990]. Subsets of data from the red unit (Undifferentiated Volcanics) and the beige unit (Cerberus Plains Unit) were analyzed using crater-counting methods to estimate their age. (b) Global context map, plotted on a 4 pixels-per-degree MOLA resolution DTM of the planet, showing study site location (outline) and proposed InSight Landing site (filled box). (c) Figure shows coverage for the main data sets used herein. The blue footprints represent the coverage of the HRSC DTM data, the green and red respectively show the spatial coverage of the CTX and HiRISE imagery used for the crater density analysis.

magnitude/frequency relationship. A paper by *Banerdt et al.* [1992] studied radial graben systems and noted that multiple methods of tectonic lithospheric deformation were required to form these features. The more recent paper by *Knapmeyer et al.* [2006] created a synthetic catalogue of seismic events. They were able to assign a distribution of events to each observed fault by first calculating an annual global budget of seismic moment release from the contraction cooling of the planet and then assuming a relationship between measured fault length and seismic moment release. However, the applicability to present-day activity is uncertain because most faults on Mars are not expected to be currently active. Therefore, specific analysis of potentially active fault zones should give a more accurate estimate.

[5] Here we adopt a regional approach and aim to quantify current seismic activity more directly. We consider the Cerberus Fossae graben systems and associated minor faults on the Elysium Planum, since this region is of particular importance for the InSight mission (Figure 1). First, it is widely accepted to be one of the youngest surfaces on Mars [*Jaeger et al.*, 2010; *Berman and Hartmann*, 2002; *Plescia*, 2003; *Vaucher et al.*, 2009], meaning that fault graben systems in the region are more likely to be representative of current seismic activity. Second, the Cerberus Fossae are located approximately 1000 km to the northeast of the proposed InSight landing site, making them a likely source of seismic signal for both the broadband seismometer and microseismometer.

[6] Our method attempts to quantify the rate of fault motion for each of the graben systems. We determine age for the youngest geological units in the area to give a maximum age for the faults, since they must be younger than any surface they bisect. Total fault motion is then determined from the available topographic data sets. The age and throw estimates are combined to give a minimum rate of motion for the faults, which we convert into an annual

seismic moment release using equation (1). This method provides a more direct measure of current fault activity than previous approaches.

2. Cerberus Fossae: Geological Context

2.1. Nature of the Cerberus Fossae

[7] The assumption that the Cerberus Fossae are tectonic graben features is fundamental to our calculations of seismic moment release. However, there is debate in the literature about the nature of these linear features; that they are either graben faults, tension cracks, or undercutting by dyke emplacement. *Burr et al.* [2002] calculated water release from the system based on two scenarios—the first is that the Fossae are caused by extension due to dyke emplacement and the second that extensional faulting is caused by flexural loading from the nearby volcanic provinces. The same mechanism is proposed by *Hall et al.* [1986]. *Carr* [2006] suggest tension cracks as a possible cause, but acknowledge that differentiation between formation scenarios is challenging from remote sensing data alone. *Pedersen et al.* [2010] suggest that v-shaped tension cracks, faulting, and flat-floored graben can all form as a result of dyke emplacement at depth—quoting the Cerberus Fossae as an example. Most other works assert that the features are graben systems [*Vetterlein and Roberts*, 2010], though still associate them with dyke emplacement or volcanism [*Ernst et al.*, 2001; *Head et al.*, 2003; *Plescia*, 2003].

[8] After reviewing the available evidence, we propose that the Cerberus Fossae are, indeed, graben faults. Their lateral extent over thousands of kilometers suggests that they are a result of dyke emplacement associated with the regional volcanic provinces. However, there are several important features suggestive of graben-forming processes, rather than simple, surface-based tension cracks. In places, it is possible to see sunken blocks of prefaulted terrain in the bottom of the Fossae. Also, topographic cross sections display uplifted footwalls, which is a diagnostic of faulting and large-scale stress fields, as opposed to cracking. If these features were tension cracks, it would preclude any ongoing seismic activity. Simple 1-D thermal modeling of lava emplacement and cooling shows that if the Cerberus Fossae were tension cracks, the emplaced flows would have long since cooled and would no longer be seismically active today. However, there is evidence of current and ongoing activity. Clear boulder trails have been identified on the Cerberus Fossae [*Roberts et al.*, 2012] showing that large objects rolled or bounced down the graben slopes. The size of these boulders would prohibit movement, unless they were disturbed by significant ground perturbation. The trails themselves also appear extremely fresh; out on the plains, similar tracks caused by rover wheels have been known to be erased in a matter of days, as dust devils and other aeolian processes deposit fresh sediment. Within the Fossae, conditions may be more sheltered, but debris slides and wind-blown dust would still tend to cover such tracks. Alternatively, it is possible that the Fossae could act as wind tunnels, funnelling strong katabatic winds down from across the plain, thus eroding the trails even faster. Either scenario implies that the most recent activity on the faults is likely to have been on the order of no more than years to decades ago and favors a graben system interpretation.

2.2. Age of the Cerberus Fossae Fault Systems

[9] Crater density analysis is a relative dating method commonly used to date planetary surfaces. It can be calibrated by radiometric dating of samples returned from the surface [*McGill*, 1977]. However, since we have no samples of a known specific origin from Mars, we must rely on isochrons modified from those developed for the Moon. These have been scaled accordingly for impactor population and predicted flux rates for Mars [*Hartmann*, 2005, 1999].

[10] Global crater-age studies, such as those by *Robbins and Hynek* [2012] and *Soderblom et al.* [1974], tend to have a minimum crater resolution of around 1.0 km. For areas such as the Cerberus Fossae, whose surfaces are extremely young, the global catalogues contain limited data. There are only four craters exceeding 1.0 km in the Cerberus Fossae region, from which little of statistical pertinence could be gained. *Jaeger et al.* [2010] determined the absolute age for the lava coating the Athabasca Valles—immediately adjacent to the Cerberus Fossae—to be >0.5 Ma based on the superposition of secondary craters from the Zunil impact and >10 Ma from similar analysis of the nearby Corinto impact. *Berman and Hartmann* [2002] quote an age of less than 20 Ma, *Burr et al.* [2002] determine deposits close to the Athabasca Valles to be "extreme Late Amazonian," and *Murray et al.* [2005] report a value of 5 ± 2 Ma. All of these estimates suggest an age for the surface around the Cerberus Fossae to be <20 Ma. We aim to validate these estimates using analysis of small craters on representative subregions for each of the units of interest.

2.3. Crater Counting: Method

[11] Dating of young surfaces like the Cerberus Fossae region requires small, subkilometer scale craters to be resolved. Therefore, we use the Context Camera (CTX) and High Resolution Imaging Science Experiment (HiRISE) data sets, which have pixel sizes of 6.0 m and 0.25 m, respectively. Figure 1c shows the distribution of CTX and HiRISE stamps found within the region of interest.

[12] Image data are analyzed using the Java Mission-planning and Analysis for Remote Sensing (JMARS) software (Figure 2). Stamps are rendered onto a geological context map of the area [*Skinner et al.*, 2006], so that different units can be identified. From this map and observation of crater densities, it is clear that two units through which the faults cut are significantly younger than the others. The craters in these units, known here as the Undifferentiated Volcanics and the Cerberus Plains Unit, as per the nomenclature used by *Plescia* [1990], are then counted using a representative subset of data, (Table 1). These data are plotted against isochrons [*Hartmann*, 2005] of crater diameter against crater density (Figure 3).

[13] Where they are particularly obvious, secondary craters are ignored since these may artificially increase the count and introduce a bias toward older estimates of age [*Werner et al.*, 2009], though there is some evidence that this is not the case. *Hartmann* [2007] argues that decimeter-sized secondaries are incorporated into the calculation of his isochrons. This means that secondaries would not necessarily bias the counts to indicate "older" ages, but may make

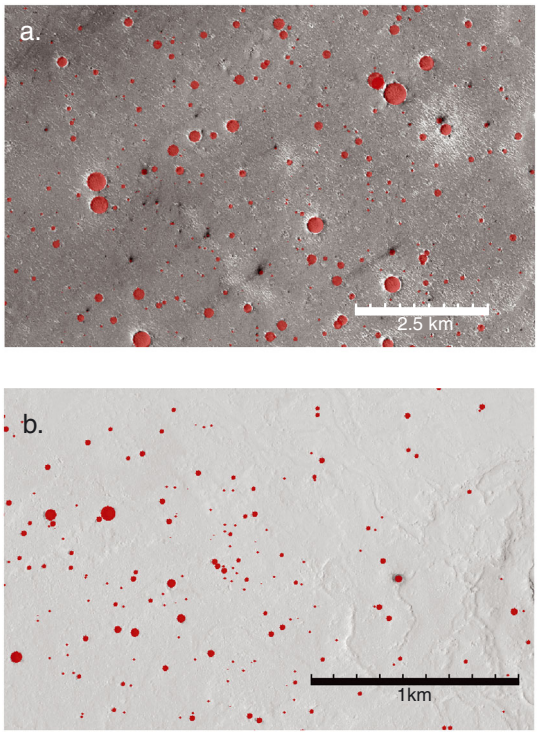

Figure 2. Example crater counting area detail. (a) CTX counting sample area from stamp P17_007698_1910_XI_11N203W which is from the Undifferentiated Volcanics Unit (156.70°E, 11.90°N). (b) HiRISE counting sample area from stamp HiRISE: ESP_016651_1895_RED which is from the Cerberus Plains Unit (161.67°E, 9.49°N).

the results of small-scale crater counts noisier. Though there is some debate as to the importance of excluding these secondaries, we err on the side of caution and particularly clustered groups, or elongate crater morphologies are assumed to be near-field secondaries and are thus ignored, on the basis that high velocity impacts tend to create circular craters, regardless of impact angle [*McEwen et al.*, 2005]. A particular source of error for the Cerberus region is the Zunil crater, which is estimated to have in excess of 10^7 secondaries greater than 15 m in diameter [*Preblich et al.*, 2007]. The number of observed elongate morphologies is significantly less than 5% of the total population, making it seemingly negligible in context of the widely accepted factor-of-two error on the calculated age estimate [*Hartmann*, 1999]; however, there will be a number of misidentified secondaries that do not fit into the elongate morphology. These craters are an important source of error for crater density statistics, but we assume that they are incorporated into the Hartmann isochrons.

2.4. Crater Counting: Results

[14] Overlapping Context Camera (CTX) and High Resolution Imaging Science Experiment (HiRISE) images are used where possible to map the crater distribution, adding confidence to the count where the size ranges coincided. It is immediately apparent from the number of craters that there is a disparate age between the Undifferentiated Volcanics and the Cerberus Plains Unit (see Table 1).

[15] When binned according to *Hartmann* [2005] and plotted against Martian isochrons (Figure 3), the data best fit an age of 500^{+500}_{-250} Ma for the Undifferentiated Volcanics and 10^{+10}_{-5} Ma for the Cerberus Plains Unit. These ages are consistent with previous estimates for the area, which agree that the lavas are no more than 0.6 Ga [*Jaeger et al.*, 2010; *Berman and Hartmann*, 2002; *Hartmann and Neukum*, 2001] with some finding units in the range 10–100 Ma [*Plescia*, 2003; *Burr et al.*, 2002]. The deficit of small craters (20–50 m) in the Undifferentiated Volcanics for the CTX counts is partially due to the difficulty of identifying very small craters which are only a few pixels wide. However, the deficit at larger scales, between 50 m and 200 m, appears to be caused by preferential infilling of smaller craters by more recent lava flows. Such resurfacing has been documented to skew results toward larger craters [*Hartmann et al.*, 1999; *Opik*, 1965]. This partial infilling could be significant, as it suggests that the age of the surface could be even younger than the value calculated.

[16] Since graben systems 1, 3, and 4 bisect the Cerberus Plains Unit, we can constrain a formation age of approximately 10 Ma for these faults. Graben system 2 does not bisect this unit and, although it likely formed contemporaneously with the other faults, we take a conservative approach and treat it as though it has the same age as the much older Undifferentiated Volcanics—approximately 500 Ma.

3. Measurement of Fault Motion

3.1. Process and Method

[17] The measurement of throw on the Cerberus Fossae is carried out using data from the High Resolution Stereo Camera (HRSC), aboard Mars Express. Stereo images collected from the instrument, which uses a "push-broom" mapping technique, have been used to construct Digital Terrain Models (DTMs) of the surface of Mars [*Gwinner et al.*, 2009]. With a maximum image resolution of 2 m and DTM resolution of 50 m [*Heipke et al.*, 2007; *Jaumann et al.*, 2007], the HRSC imagery is the optimal compromise between resolution and spatial coverage for our study (Figure 1c), since none of the higher-resolution HiRISE DTMs are available in this region. The global MOLA DTM data set is used as a way of corroborating the findings of the HRSC data, though it too has limitations. The low density of MOLA orbital tracks in equatorial regions and the large footprint of the laser means that in places the topographic differences are underestimated from the MOLA data, especially for the relatively narrow fossae. The same fault mapping techniques and data processing are applied to both data sets, not only to increase confidence in the results but also to compensate for the incomplete coverage of the HRSC data.

[18] In order to analyze the graben systems and minor faults, the DTMs are filtered using a Sobel edge-detection filter to pick out the sharp changes in topography [*Argialas and Mavrantza*, 2004]. Manual mapping of the faults is used to construct topographic profiles normal to the line of the faults every 200 m (Figure 4a). We then average topography adjacent to the graben and use this to create a linear interpolation of prefaulted topography across the faults. The standard deviation of the topographic variation is used to construct an error envelope, which we plot on the throw profiles. The height difference between the prefaulted

Table 1. Summary of Crater Counting for CTX and HiRISE Test Areas[a]

			Undifferentiated Volcanics (Red Unit)	Cerberus Plains Unit (Beige Unit)
CTX Data	General	Stamp ID	P17_007698_1910_XI_11N203W	G05_020119_1895_XN_09N198W
		Area analyzed (km^2)	810.37	772.64
		Total number of craters	5753	594
	Data bin midpoints	Midpoint (m)	Nbin	Nbin
		9.27	164	53
		13.1	46	11
		18.57	1005	165
		26.26	1171	206
		37.14	1146	94
		52.56	838	47
		74.29	546	14
		105.06	411	3
		148.32	245	1
		209.76	123	0
		297.07	44	0
		420.12	10	0
		594.56	2	0
		1187.43	2	0
HiRISE Data	General	Stamp ID	ESP_016216_1900_RED	ESP_106651_1895_RED
		Area analyzed (km^2)	14.64	6.42
		Total number of craters	5337	1290
	Data bin midpoints	Midpoint (m)	Nbin	Nbin
		4.64	2514	748
		6.57	1259	307
		9.27	831	170
		13.1	471	61
		18.57	181	4
		26.26	48	0
		37.14	25	0
		52.56	5	0
		74.29	3	0

[a]Crater bins are the same as those defined for *Hartmann* [2005].

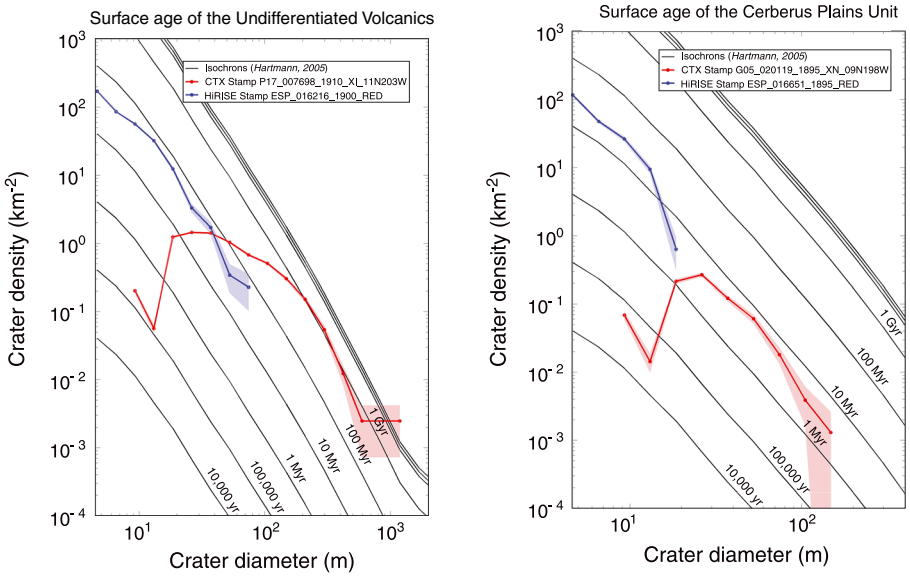

Figure 3. Martian isochron plots following *Hartmann* [2005] showing a size-frequency distribution of craters. Black solid lines show isochrons. Results from CTX (red) and HiRISE (blue), error bars given by $\sqrt{n}$. assuming Poisson counting statistics. (a) Data for the Undifferentiated Volcanics, showing an age of approximately 500 Ma. (b) Data for the Cerberus Plains Unit, showing an age of approximately 10 Ma. The sharp dropoff around 20 m in CTX counts for both the Undifferentiated Volcanics and Cerberus Plains Unit is due to the difficulty in resolving craters smaller than this, since they consist of 4 or fewer pixels. The more gentle roll-off observed in the CTX data for craters between about 50 m and 200 m for the UV unit is likely caused by the infilling of small craters by later lava flows and aeolian deposition.

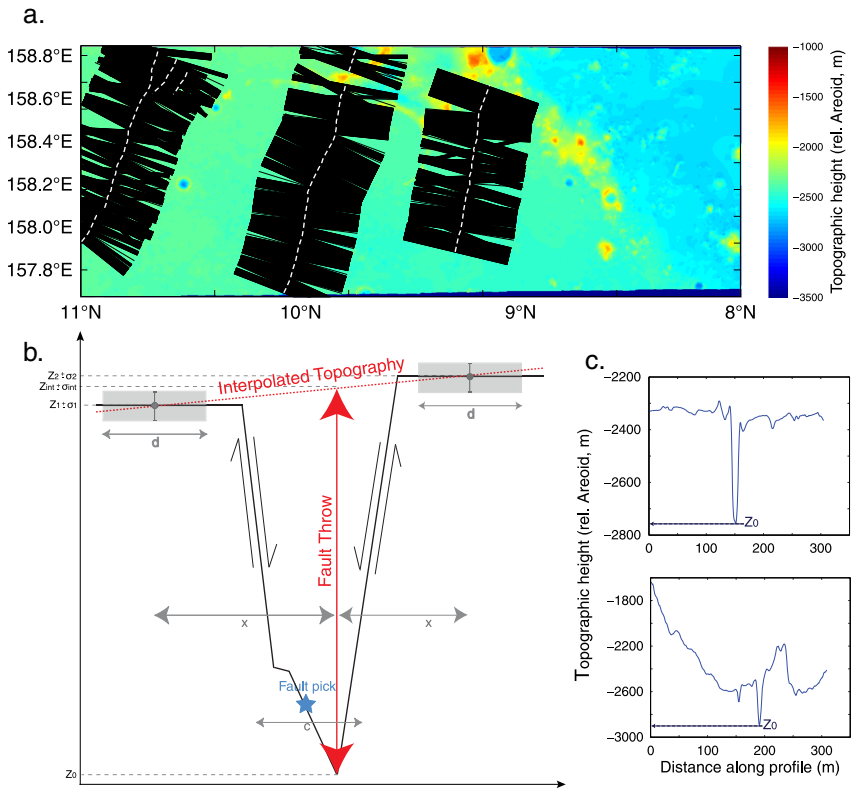

Figure 4. Method of determination of fault throw across a graben. (a) Lines of the mapped faults are shown in white with dense sampling of perpendicular profiles plotted onto a HRSC DTM. (b) Schematic showing the process of topographic interpolation and throw calculation. The minimum topography value [Z_0] on the graben hanging wall is found within the range [c] from the fault pick point. A specified distance [x] is moved away from this point, before the mean and standard deviation across a range [d] are calculated on the surrounding topography. The averaged topography either side of the fault is then linearly interpolated and the difference between this interpolated value [Z_{int}] and the minima [Z_0] is calculated to give the throw [T]. Errors [σ] are calculated from the standard deviation on the surrounding topography. (c) Two examples of profiles plotted from graben system 1, the northernmost of the fossae. Figure 4c (top) shows a profile with little topographic variation, which will result in a small error envelope. Figure 4c (bottom) shows a more variable profile which will result in a greater standard deviation and error in throw calculation.

interpolated topography and the present topographic minima on the graben hanging wall is taken to be the throw on the faults (Figure 4b).

3.2. Measured Throws: Results

[19] Figure 5 shows the variation in throw along the fault system. In most cases, there is good agreement between HRSC and MOLA topography data. In places, there is a large discrepancy, but close investigation of these areas shows that the faults are not resolved in the MOLA data. The width of the fossae are at the limit of the MOLA resolution in some areas, making measurements of throw in these areas an underestimate. In cases where the faults are obviously unresolved, the MOLA data is masked from Figure 5, leaving only the places where the MOLA DTM is fully or partially resolved. This largely removes the areas of discrepancy between the data sets; however, there are still segments where the HRSC and MOLA seem not to correspond. At around 158°E on graben system 2, there is a discrepancy of over 300 m between the two, though the shape of the topographic variation is the same. Inspection of imagery data suggests that this could be caused by the presence of several small en echelon features at this point, resulting in incorrect picks of hanging wall minima by the automated profiling process. In the places where resolved MOLA data exist, but there are gaps in the HRSC coverage, the error on the MOLA DTM is large enough that we prefer to take the maximum observed throw from the fully resolved HRSC data for each graben.

[20] The Northern and Southern Cerberus Fossae, Graben 1 and 2, respectively, both have large observed vertical offsets. Graben 1, the Northernmost Fossa, has a maximum observed throw of 1092 ± 88.2 m and the Southern Fossa, Graben 2, has a maximum throw of 615±6.3 m. Both graben seem to have their peak throws toward the center of the system, with lower observed throw at the extremities. This trend is visible on both the HRSC and MOLA topography data sets for Graben 1 and 2, with the exception of the easternmost edge of Graben 2, where the faults pass through an inlier of a much older terrain, propagating though thicker crust. Though some variation is expected as a result of variable erosion rates, this tail-off toward the fault terminus

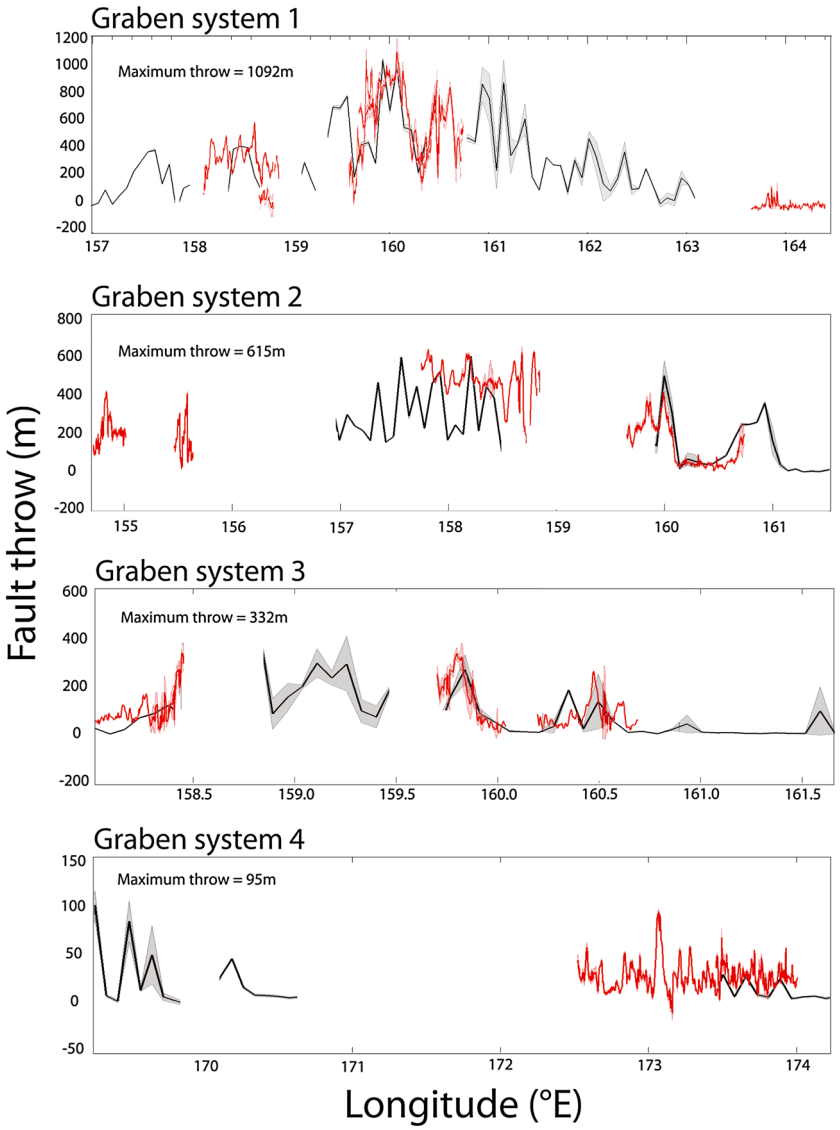

Figure 5. Variation in throw along each of the four graben systems of the Cerberus Fossae. 128 pixels per degree resolution MOLA and 50 m HRSC-based throw measurements are shown. MOLA data provide a low resolution along fault profile, with error envelopes shaded in grey. HRSC throw calculations are shown in red with red error envelopes. HRSC data have less spatial coverage and the gaps in the profile correspond to lack of stamp data coverage, but, in general, it is much more reliable, since the faults are fully resolved in all cases. At these latitudes and with a strike of 113°, 1° of latitude is equivalent to 143.94 km along the fault trace.

is consistent with observed terrestrial behavior of outward-propagating fault systems [*Peacock and Sanderson*, 1991]. The throw measured on the two more minor fault systems is much lower. Graben 3 has a maximum throw of 332 ± 41.2 m, when measured according to the HRSC data and Graben 4 has a maximum throw of just 95 ± 2.7 m. The throw variation on Graben 4 is chaotic along the profile, and there is no real discernible trend.

[21] Errors in the throw measurement come primarily from variation in topography adjacent to the fault. Uncertainty in vertical resolution also arises from the way the HRSC DTM data set is made. The DTMs are constructed using stereo image pairs, and are tied to the MOLA-determined topography [*Gwinner et al.*, 2010]. The height accuracy of a single pixel is at least 12.5 m [*Gwinner et al.*, 2010], with some generation algorithms reaching 10 m [*Jaumann et al.*, 2007] or even 6–8 m [*Kim and Muller*, 2008]. This 10 m error is negligible in comparison with uncertainty introduced by topographic variations adjacent to the fault, therefore, standard deviation of this topographic variation is used to create error envelopes which are plotted with the data (Figure 5).

4. Assessment of Seismic Activity

4.1. Estimated Moment Release

[22] The rate of fault motion is calculated by combining the new surface ages, determined from crater density analysis and the measurement of maximum observed throw. This

Table 2. Summary of Data and Calculation Results of Annual Seismic Moment Release on Each Graben System

	Graben 1	Graben 2	Graben 3	Graben 4
Surface age (Ma)	10^{+10}_{-5}	500^{+500}_{-250}	10^{+10}_{-5}	10^{+10}_{-5}
Fault length (km)	578.75	488.08	224.21	404.64
Fault depth (km)	50 ±12	50 ±12	50 ±12	50 ±12
Maximum observed throw, S_{MAX} (m)	1092 ± 88.2	615 ± 6.3	332 ± 41.2	95 ± 2.7
Length-averaged slip, $\bar{s}$ (m)	546 ± 44.1	308 ± 3.15	166 ± 20.6	48 ± 1.35
μ_{MARS} (Pa)	$3 \pm 1 \times 10^{10}$	$3 \pm 1 \times 10^{10}$	$3 \pm 1 \times 10^{10}$	$3 \pm 1 \times 10^{10}$
M_0 per graben (Nm)	$9.5 \pm 4.0 \times 10^{23}$	$4.5 \pm 1.9 \times 10^{23}$	$1.2 \pm 0.5 \times 10^{23}$	$5.8 \pm 2.4 \times 10^{22}$
Annual moment release (Nm/yr)	$9.5^{+10.3}_{-6.2} \times 10^{16}$	$9.0^{+9.7}_{-5.8} \times 10^{14}$	$1.2^{+1.3}_{-0.8} \times 10^{16}$	$5.8^{+6.2}_{-3.7} \times 10^{15}$
Moment magnitude equivalent (M_W)	5.46 - 4.95	4.12 - 3.60	4.87 - 4.35	4.65 - 4.14

is then converted into a total cumulative moment release on each fault, integrated over their assumed ages. In order to do this, we assume a uniform temporal distribution of activity since the fault genesis. We consider this a reasonable assumption, since it is likely that a feature of this size was formed gradually, over geological timescales. There is also evidence of a long history of activity, certainly through the Amazonian, as shown by *Vetterlein and Roberts* [2010]. The total moment release, M_0 over the age of the faults is given by the following:

$$M_0 = \mu A \bar{s}, \quad (1)$$

where μ is the shear modulus, A is the fault surface area and $\bar{s}$ is the total length-averaged slip. For Mars, μ is generally thought to lie between 20 and 40 GPa [*Knapmeyer et al.*, 2006; *Grott et al.*, 2005; *Schultz*, 2003; *Turcotte et al.*, 2002], taken here to be 30 ± 10 GPa. A is calculated from fault length, L and assumed fault depth, D. The relationship governing the ratio of fault depth to length in analogous terrestrial intraplate settings of normal and strike slip faults is given by *Leonard* [2010]:

$$D = 1.7L^{2/3}. \quad (2)$$

However, given the large (>1000 km) lateral extent of the fault system, this calculation results in unphysical estimates of faulting depth. In all cases, the calculated depth exceeds the depth estimated for the elastic thickness of the lithosphere of the Elysium Planitia, of around 50 km (20–50 km [*Comer et al.*, 1985], 50 ± 12 km [*Wieczorek and Zuber*, 2004], and 56 ± 20 km [*Belleguic et al.*, 2005]). We, therefore, limit the depth of each fault to the depth of the elastic thickness in the region—50 km; a reasonable estimate for a major graben system of this kind. There is evidence that the faults may be segmented, which would affect the depth of faulting. Treating the segments as individual faults would significantly decrease the faulted depth. However, recent work by *Hauber et al.* [2013] shows that as fault segments like this grow, they approach the character of a single fault. Work by *Vetterlein and Roberts* [2010, Figure 3] also shows that the Cerberus Fossae segments appear to behave as a single fault system in terms of the displacement length profile. We, therefore, assume the segments to be fully linked and treat them as such when determining depth of faulting.

[23] Though it is impossible to quantify the extent to which aeolian, and perhaps fluvial, processes have eroded the faults, the generic terrestrial longitudinal fault profile [*Scholz et al.*, 1993] can be used to predict that the length-averaged slip, $\bar{s}$ is approximately half of the maximum observed throw, S_{MAX}. Taking $\bar{s} = S_{MAX}/2$ will lead to a conservative estimate of slip rate that assumes no erosion, consistent with the aim of providing a lower-bound estimate of moment release rate. It should be noted that this length-averaged slip was doubled in the calculation to account for the dual nature of a graben system, which has two parallel antidipping faults.

[24] Using these figures of measured fault lengths and length-averaged slip, the total cumulative moment release on each of the graben systems is calculated to be 0.5–9.5 × 10^{23} Nm (see Table 2). The summed moment release rates represent a total annual seismic moment release of $1.14^{+1.04}_{-0.62} \times 10^{17}$ Nm/yr, assuming all energy is released seismically and that there is no strike-slip component of motion (Figure 6).

[25] This figure is striking since it is comparable to *global* annual moment budgets calculated in other works (10^{18} Nm/yr [*Golombek et al.*, 1992], 3.42 × 10^{16} to 4.78 × 10^{18} Nm/yr [*Knapmeyer et al.*, 2006]), implying that Mars could be more seismically active than previous estimates suggest or that the fault depth has been overestimated (see section 5.2).

[26] One potential source of error is the possibility that the faults may no longer be active or that motion is taken

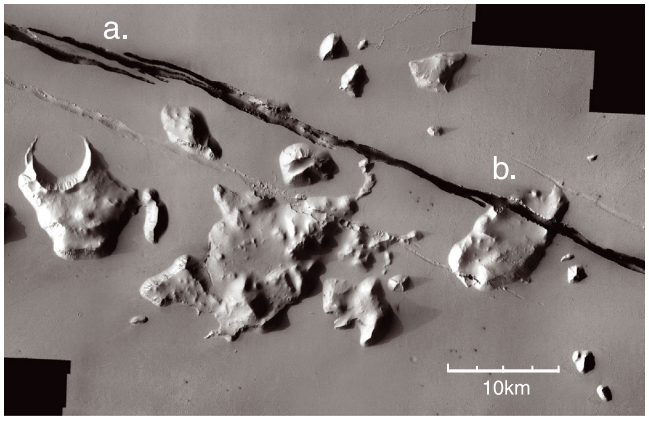

Figure 6. Composite THEMIS image of the Cerberus Fossae, (15 °N, 170 °E [*NASA/JPL-Caltech/ASU*]), showing two features of interest. (a) Fault segmentation and en echelon features could result in overestimate of moment release. However, faults are likely to conjoin at depth, minimizing the effect of this error. (b) Preexisting mesa, bisected by one of the graben systems. It is clear that there has been little to no horizontal component of strike-slip motion on these faults.

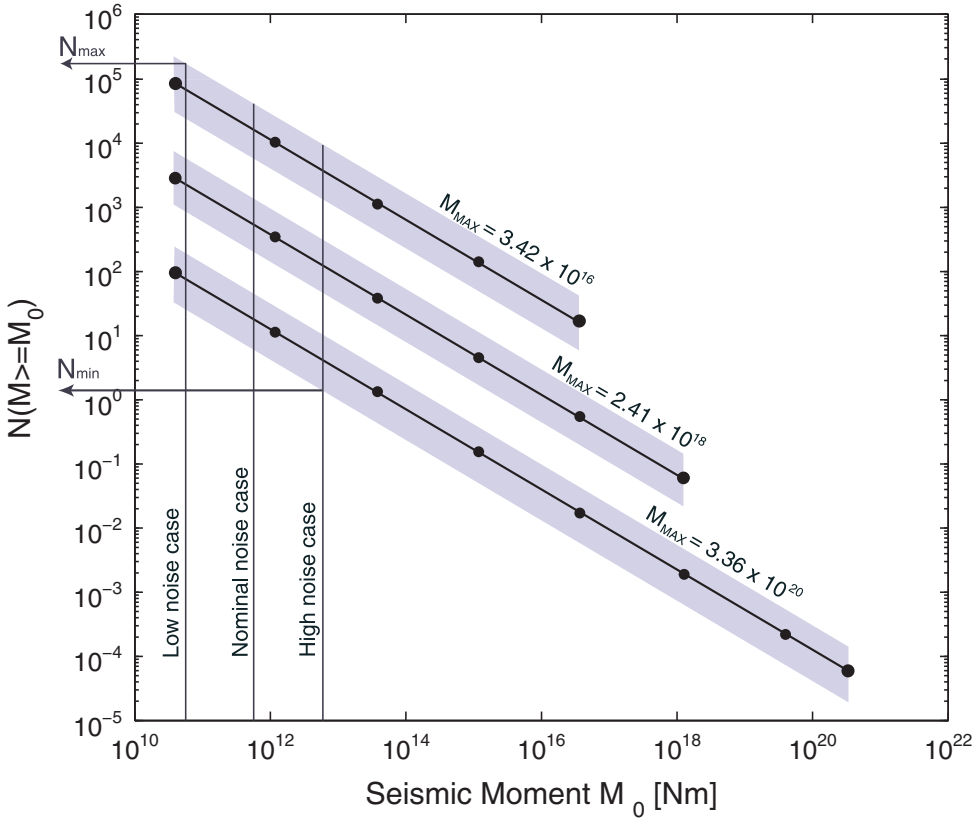

Figure 7. Modified from *Knapmeyer et al.* [2006], showing the predicted size-frequency distribution of seismic events. Calculations are based on the assumptions of *Knapmeyer et al.* [2006]; that $\beta = 0.625$, the minimum detectable event size is equivalent to an $M_W = 1$, with moment release of 4×10^{10} Nm and that the maximum event size depends on the strength of the seismogenic lithosphere and is varied between 3.42×10^{16}, 2.41×10^{18}, and 3.36×10^{20} Nm. Error envelopes, shaded, are calculated by propagating error from uncertainties in surface age estimates, fault depth, and observed throw. Detectability criteria for low, nominal, and high noise cases are shown. The minimum number of detectable events [$N_{\min}$] predicted to occur within one Earth year is 1.5. The maximum number of detectable events is predicted to be 1.9×10^5. This means that within the nominal mission lifetime of one Martian year, we expect to see between 2.7 and 3.5×10^5 detectable events.

up aseismically. There seems, however, to be compelling evidence that Cerberus Fossae are still active (with boulder trails and geologically recent volcanic and aqueous activity) and that the energy is released in discrete seismic events. The Martian crust itself is cold and rigid, capable of supporting the huge edifice of Olympus Mons for several billion years [*Arkani-Hamed and Riendler*, 2002]. This makes aseismic motion close to the surface or on faults with a surface expression, unlikely.

4.2. Event Detectability at InSight

[27] In order to determine detectability of seismic events, an estimate of the number of events, noise environment, and instrument performance are required. The number of seismic events occurring on the Cerberus Fossae over the course of a year is determined using a Gütenberg-Richter law to distribute the moment release over a size-frequency probability function. *Knapmeyer et al.* [2006] constructed several different models of Martian seismicity using this relationship and different estimates of global seismicity. Here we scale the models calculated by *Knapmeyer et al.* [2006] to the moment release for the Cerberus Fossae region. We used the same minimum event size of 3.981×10^{10} Nm ($M_W = 1$) and vary the maximum possible event size; using 3.4×10^{16} Nm ($M_W = 4.95$), 2.4×10^{18} ($M_W = 6.19$), and 3.4×10^{20} ($M_W = 7.62$) in the same way. For example, for a 1000 km long fault, with a faulting depth of 50 km, a $M_W = 3$ event would be equivalent to a slip of 2.65×10^{-8} m over the entire length of the fault and a $M_W = 5$ event would be equivalent to a slip of 2.65×10^{-5} m over the entire length of the fault.

[28] The distributions are plotted (Figure 7), with each curve showing the same total moment release, but scaled for different maximum event sizes. The gradient of the curve is given by the relationship $\beta = 2/3b$, where b is the terrestrial Gütenberg-Richter prediction for the distribution of event sizes. On the Earth, it is generally assumed to be 1 [e.g., *Goins and Lazarewicz*, 1979], but *Kagan* [1997, 1999, 2002a, 2002b] finds the value to be lower (between 0.60 and 0.65), almost universally. We follow *Knapmeyer et al.* [2006], who assume a β value of 0.625 based on the midpoint of this range.

Table 3. Minimum Required Noise Performance Capabilities of the SEIS Instruments and the Sizes of the Minimum Detectable Event at an Epicentral Distance Equivalent to the Source-Receiver Distance Between the Cerberus Fossae and the InSight Landing Site

	n_{RMS} ($m/s^2/\sqrt{Hz}$)	Minimum Detectable M_0 (Nm)	M_W Equivalent
High noise	1.0×10^{-8}	4.74×10^{12}	2.4
Nominal noise	1.0×10^{-9}	4.74×10^{11}	1.7
Low noise	1.0×10^{-10}	4.74×10^{10}	1.1

[29] In order to estimate instrument capability, the currently defined required noise floor performances of the InSight SEIS instruments [SP (1×10^{-8} $m/s^2/\sqrt{Hz}$) and VBB ($1 \times 10^{-9} m/s^2/\sqrt{Hz}$) (T. Pike and P. Lognonné, personal communication, 2013)] are used to determine the capability at the source-receiver distance of 1000 km (approximately 20°). These performances were defined based on expected ambient noise levels for Mars [*Lognonné and Mosser*, 1993]. Using the waveform modeling of *Teanby and Wookey* [2011, Figure 11], which shows the maximum *P* wave amplitude against source-receiver offset, we define a minimum moment detectability criteria, M_{detect}. We assume that an event is detectable using *P* waves if the predicted amplitude of its signal at the source-receiver distance exceeded the peak band noise;

$$n_{peak} = 1.25 n_{RMS} \sqrt{(f_2 - f_1)}, \quad (3)$$

where the frequency range f_2–f_1 is taken to be 0.4–4 Hz, which includes most of the energy from *P* mode body waves [*Teanby and Wookey*, 2011]. In this frequency range, the amplitude scales linearly with seismic moment. Therefore, taking a reference event, for example, a moment of 10^{12} Nm (M_W = 1.93) at an epicentral distance of 20° (the source-receiver distance from the Cerberus Fossae to the proposed InSight landing site), we can define an expression for the amplitude, *a*, of the acceleration at the receiver in the 0.4–4 Hz frequency range::

$$a(\Delta = 20°, M) = a(\Delta = 20°, M = 10^{12}\text{Nm}) \times \frac{M}{10^{12}}. \quad (4)$$

[30] The reference amplitude, $a(\Delta = 20°, M = 10^{12}\text{Nm})$, for an event of this size, at the given epicentral distance is $5 \times 10^{-9} m/s^2$ [*Teanby and Wookey*, 2011, Figure 11]. We substitute this into equations (3) and (4) and set $a = n_{peak}$ to define our detectability criterion, M_{detect}:

$$M_{detect} = 2 \times 10^{20} \times n_{RMS}. \quad (5)$$

[31] If n_{RMS} is $10^{-8} m/s^2/\sqrt{Hz}$ for InSight SEIS SP, $10^{-9} m/s^2/\sqrt{Hz}$ for SEIS VBB and $10^{-10} m/s^2/\sqrt{Hz}$ in an optimistic estimate of noise floor for the VBB, then we can define these to be our high, nominal, and low noise conditions for detectability at the InSight landing site (Table 3). The minimal detectable event sizes for each noise condition are shown on Figure 7. This determines the number of events, of this size or larger, generated at the Cerberus Fossae each year whose amplitudes would be detectable at the InSight landing site.

[32] The estimated number of annually detectable events is between 1.5×10^0 and 1.9×10^5 . This represents a conservative estimate of number of annually detectable events and is strongly dependent on maximum defined event size. In even the most pessimistic case of high noise level, with the annual moment release spread over the widest range of possible event sizes, we would still expect to see *P* wave arrivals from the Cerberus Fossae with sufficient amplitude to be detected over the 2 year nominal mission lifetime.

5. Discussion

5.1. Nature of the Cerberus Fossae

[33] Throughout this paper, we have assumed the Cerberus Fossae to be tectonically active graben systems. There is good evidence to suggest that this is the case. First, the global scale of the features, which extend for more than 1000 km, is suggestive of large-scale tectonic stresses. Second, the morphology of the fissures themselves is suggestive of terrestrial graben; in places, sunken blocks and other prefaulted terrain are visible [*Vetterlein and Roberts*, 2010] on the floor of the Fossae; additionally, many of the topographic sections extracted perpendicular to the Fossae show evidence of footwall uplift. There is also the evidence of ongoing activity to consider. Boulder trails observed by *Roberts et al.* [2012] suggest that the area around the Cerberus Fossae undergoes significant ground perturbation. However, it is impossible to be certain of the exact nature and activity of the Cerberus Fossae solely from orbital imagery. Further constraints will be possible with InSight.

5.2. Depth of Faulting

[34] Assumed fault depth has a direct effect on calculated moment release. The depth of faulting of 50 km used in our calculations was derived from our assumption that each of the Fossae act as a single fault system, even though, in places, it is possible to see evidence of segmentation. Work by *Hauber et al.* [2013] shows that in the case of a segmented fault system, the displacement:length ratio more closely matches ratios from terrestrial faults when treated as a single feature. *Vetterlein and Roberts* [2010] also show that the displacement profile for the Cerberus Fossae themselves resembles that of a single fault. It is for this reason that we feel able to use length to depth scaling relationships given for analogous terrestrial faults to estimate the depth of faulting. However, as the result of these calculations give unphysical estimates of depth, we limit the depth of faulting to the elastic thickness of the lithosphere in the region, estimated at around 50 km [*Comer et al.*, 1985; *Wieczorek and Zuber*, 2004; *Belleguic et al.*, 2005]. However, the results of our moment calculations are simple to adjust for other assumed fault depths: the moment release is linearly scalable with the depth of faulting. The curves shown on Figure 7

can be shifted up and down to vary with depth. For example, if the depth of faulting was much shallower on the order of the observed throw on the faults, then the annual moment release would be lower by two orders of magnitude. For example, if we take a faulting depth of 1 ± 0.5 km, then this will result in an annual moment release of $2.25^{+2.24}_{-1.50} \times 10^{15}$ Nm/yr—equivalent to a single event of magnitude 3.85–4.40. Shallower faulting would also allow less crustal stress to build up so would result in a reduced maximum event size and more frequent smaller events.

5.3. Distribution of Seismic Activity Through Time

[35] In calculating an annual moment release, the total moment release for each fault system has been linearly distributed through time. This was considered to be the simplest and most appropriate assumption, though it is possible that activity has varied through time. Features on this scale are unlikely to have formed quickly and catastrophically; it is much more likely that they have grown gradually over geological time. *Vetterlein and Roberts* [2010] present evidence that the Fossae have been active through the Amazonian, which supports our assumption. Considering the uncertainty in the nature of the Cerberus Fossae, we feel that any more complex assumption would at present be extremely underdetermined.

6. Conclusions

[36] Assuming that the faults of the Cerberus Fossae have been active for the past 10 Myr and remain active today, our calculations show that this area alone generates an annual seismic moment release of $1.14^{+1.04}_{-0.62} \times 10^{17}$ Nm. We would expect to see an annual detectable seismicity rate of 1.5×10^0 to 1.9×10^5—that is between 2.7×10^0 and 3.5×10^5 events over the course of the InSight nominal mission lifetime of 669 sols. The implication for InSight of this number of events would be significant. To detect between 2.7×10^0 and 3.5×10^5 seismic events over the nominal mission period would have a large impact, in particular, on the SEIS instrument payload. On the other hand, the absence of this seismicity would also help to determine the nature of the Cerberus Fossae, distinguishing between the possibility that they are tension cracks and our assumption that they are tectonically active fault systems.

[37] The mission science objectives include the determination of the size, composition and physical state of the core, thickness, and structure of the crust and composition and structure of the mantle; all of which require seismic activity. At an approximate epicentral distance of 20°, we predict that the Cerberus Fossae will be an extremely important source for upper mantle and crustal exploration.

[38] **Acknowledgments.** This research was funded by the Natural Environment Research Council (NERC), the Leverhulme Trust, the Science and Technology Facilities Council (STFC), and the European Research Council (ERC). This work has received funding from the European Research Council under the European Unions Seventh Framework Programme (FP7/2007-2013)/ERC Grant agreement no. 240473 "CoMITAC".

References

Anderson, R. C., J. M. Dohm, M. P. Golombek, A. F. C. Haldemann, B. J. Franklin, K. L. Tanaka, J. Lian, and B. Peer (2001), Primary centers and secondary concentrations of tectonic activity through time in the western hemisphere of Mars, *J. Geophys. Res.*, *106*(E9), 20,563–20,58.

Argialas, D. P., and O. D. Mavrantza (2004), Comparison of edge detection and Hough transform techniques for the extraction of geologic features, *Int. Arch. Photogramm. Remote Sens. Spatial Inf. Sci.*, *34*, 12–23.

Arkani-Hamed, J., and L. Riendler (2002), Stress differences in the Martian lithosphere: Constraints on the thermal state of Mars, *J. Geophys. Res.*, *107*(E12), 5119, doi:10.1029/2002JE001851.

Banerdt, B. (2010), Innovative approaches for seismic studies of Mars (Invited), Abstract U41A-04 presented at 2010 Fall Meeting, AGU, San Francisco, Calif.

Banerdt, W., M. P. Golombek, and K. L. Tanaka (1992), Stress and tectonics on Mars, *Mars*, *1*, 249–297.

Belleguic, V., P. Lognonné, and M. Wieczorek (2005), Constraints on the Martian lithosphere from gravity and topography data, *J. Geophys. Res.*, *110*, E11005, doi:10.1029/2005JE002437.

Berman, D. C., and W. K. Hartmann (2002), Recent fluvial, volcanic, and tectonic activity on the Cerberus plains of Mars, *Icarus*, *159*(1), 1–17.

Burr, D. M., J. A. Grier, A. S. McEwen, and L. P. Keszthelyi (2002), Repeated aqueous flooding from the Cerberus Fossae: Evidence for very recently extant, deep groundwater on Mars, *Icarus*, *159*, 53–73.

Carr, M. H. (2006), *The Surface of Mars*, Cambridge Univ. Press, New York.

Comer, R. P., S. C. Solomon, and J. W. Head (1985), Mars: Thickness of the lithosphere from the tectonic response to volcanic loads, *Rev. Geophys.*, *23*(1), 61–92.

Davis, P. M. (1993), Meteoroid impacts as seismic sources on Mars, *Icarus*, *105*, 469–478.

Ernst, R. E., E. B. Grosfils, and D. Mège (2001), Giant dike swarms: Earth, Venus, and Mars, *Annu. Rev. Earth Planet. Sci.*, *29*, 489–534.

Goins, N. R., and A. R. Lazarewicz (1979), Martian seismicity, *Geophys. Res. Lett.*, *6*, 368–370.

Golombek, M. P., W. B. Banerdt, K. L. Tanaka, and D. M. Tralli (1992), A prediction of Mars seismicity from surface faulting, *Science*, *258*(5084), 979–981.

Grott, M., E. Hauber, S. C. Werner, P. Kronberg, and G. Neukum (2005), High heat flux on ancient Mars: Evidence from rift flank uplift at Coracis Fossae, *Geophys. Res. Lett.*, *32*, L21201, doi:10.1029/2005GL023894.

Gwinner, K., F. Scholten, F. Preusker, S. Elgner, T. Roatsch, M. Spiegel, R. Schmidt, J. Oberst, R. Jaumann, and C. Heipke (2010), Topography of Mars from global mapping by HRSC high-resolution digital terrain models and orthoimages: Characteristics and performance, *Earth Planet. Sci. Lett.*, *294*, 506–519.

Gwinner, K., F. Scholten, M. Spiegel, R. Schmidt, B. Geise, J. Oberst, C. Heipke, R. Jaumann, and G. Neukum (2009), Data validation of high-resolution digital terrain models from Mars Express HRSC Data, *Photogramm. Eng. Remote Sens.*, *75*(9), 1127–1142.

Hall, J. L., S. C. Solomon, and J. Head (1986), Elysium Region, Mars: Tests of lithospheric loading models for the formation of tectonic features, *J. Geophys. Res.*, *91*(B11), 11,377–11,392.

Hartmann, W. K. (1999), Martian cratering VI: Crater count isochrons and evidence for recent volcanism from Mars Global Surveyor, *Meteorit. Planet. Sci.*, *34*, 167–177.

Hartmann, W. K. (2005), Martian cratering 8: Isochron refinement and the chronology of Mars, *Icarus*, *174*, 294–320.

Hartmann, W. K. (2007), Martian cratering 9: Toward resolution of the controversy about small craters, *Icarus*, *189*, 274–278.

Hartmann, W. K., M. Malin, A. McEwen, M. Carr, L. Soderblom, P. Thomas, E. Danielson, P. James, and J. Veverka (1999), Evidence for recent volcanism on Mars from crater counts, *Nature*, *397*, 586–589.

Hartmann, W. K., and G. Neukum (2001), Cratering chronology and the evolution of Mars, *Space Sci. Rev.*, *96*, 165–194.

Hauber, E., M. Voelker, K. Gwinner, M. Knapmeyer, M. Grott, and K.-D. Matz (2013), Fault scaling on Mars: Slip distribution and displacement length relationship derived from HRSC data, *Eur. Planet. Sci. Congress*, *8*, EPSC2013-987.

Head, J. W., L. Wilson, and K. L. Mitchell (2003), Generation of recent massive water floods at Cerberus Fossae, Mars by dike emplacement, cryospheric cracking, and confined aquifer groundwater release, *Geophys. Res. Lett.*, *30*(11), 1577, doi:10.1029/2003GL017135.

Heipke, C., et al. (2007), Evaluating planetary digital terrain models—The HRSC DTM test, *Planet. Space Sci.*, *55*, 2173–2191.

Jaeger, W. L., et al. (2010), Emplacement of the youngest flood lava on Mars: A short, turbulent story, *Icarus*, *205*, 230–243.

Jaumann, R., et al. (2007), The high-resolution stereo camera (HRSC) experiment on Mars Express: Instrument aspects and experiment conduct from interplanetary cruise through the nominal mission, *Planet. Space Sci.*, *55*, 928–952.

Kagan, Y. Y. (1997), Seismic moment-frequency relation for shallow earthquakes: Regional comparison, *J. Geophys. Res.*, *102*, 2835–2852.

Kagan, Y. Y. (1999), Universality of the seismic moment-frequency relation, *Pure Appl. Geophys.*, *155*, 537–573.

Kagan, Y. Y. (2002a), Seismic moment distribution revisited: I. Statistical results, *Geophys. J. Int.*, *148*, 520–541.

Kagan, Y. Y. (2002b), Seismic moment distribution revisited: II. Moment conservation principle, *Geophys. J. Int.*, *149*, 731–754.

Kim, J. R., and J.-P. Muller (2008), Very high resolution stereo DTM extraction and its application to surface roughness estimation over Martian surface, *Int. Arch. Photogramm. Remote Sens. Spatial Inf. Sci.*, *37*(B4), 993–998.

Knapmeyer, M., J. Oberst, E. Hauber, M. Wählisch, C. Deuchler, and R. Wagner (2006), Working models for spatial distribution and level of Mars' seismicity, *J. Geophys. Res.*, *111*, E11006, doi:10.1029/2006JE002708.

Leonard, M. (2010), Earthquake fault scaling: Self-consistent relating of rupture length, width, average displacement and moment release, *Bull. Seismol. Soc. Am.*, *100*(5A), 1971–1988.

Lognonné, P. (2005), Planetary seismology, *Annu. Rev. Earth Planet. Sci.*, *33*(1), 571–604.

Lognonné, P. (2009), Seismic waves from atmospheric sources and atmospheric/ionospheric signatures of seismic waves, in *Infrasound Monitoring for Atmospheric Studies*, edited by A. Le Pichon, E. Blanc, and A. Hauchecorne, pp. 281–304, Springer, Netherlands.

Lognonné, P., and B. Mosser (1993), Planetary seismology, *Surv. Geophys.*, *14*, 239–302.

McEwen, A., B. S. Preblich, E. P. Turtle, N. A. Artemieva, M. P. Golombek, M. Hurst, R. L. Kirk, D. M. Burr, and P. R. Christensen (2005), The rayed crater Zunil and interpretations of small impact craters on Mars, *Icarus*, *176*(2), 351–381.

McGill, G. E. (1977), Craters as "fossils": The remote dating of planetary surface materials, *Geol. Soc. Am. Bull.*, *88*, 1102–1110.

Murray, J. B., et al. (2005), Evidence from the Mars Express High Resolution Stereo Camera for a frozen sea close to Mars' equator, *Nature*, *434*, 352–256.

Opik, E. J. (1965), Mariner IV and craters on Mars, *Irish Astron. J.*, *7*, 92.

Peacock, D. C. P., and D. J. Sanderson (1991), Displacements, segment linkage and relay ramps in normal fault zones, *J. Struct. Geol.*, *13*(6), 721–733.

Pedersen, G. B. M., J. W. Head, and L. Wilson (2010), Formation, erosion and exposure of Early Amazonian dikes, dike swarms and possible subglacial eruptions in the Elysium Rise/Utopia Basin Region, Mars, *Earth Planet. Sci. Lett.*, *294*(3-4), 424–439.

Plescia, J. B. (1990), Recent flood lavas in the Elysium region of Mars, *Icarus*, *88*(2), 465–490.

Plescia, J. B. (2003), Cerberus Fossae, Elysium, Mars: A source for lava and water, *Icarus*, *164*, 79–95.

Preblich, B. S., A. S. McEwen, and D. M. Studer (2007), Mapping rays and secondary craters from the Martian crater Zunil, *J. Geophys. Res.*, *112*, E05006, doi:10.1029/2006JE002817.

Robbins, S. J., and B. M. Hynek (2012), A new global database of Mars impact craters $\geq$1 km: 2. Global crater properties and regional variations of the simple-to-complex transition diameter, *J. Geophys. Res.*, *117*, E06001, doi:10.1029/2011JE003967.

Roberts, G. P., B. Matthews, C. Bristow, L. Guerrieri, and J. Vetterlein (2012), Possible evidence of paleomarsquakes from fallen boulder populations, Cerberus Fossae, Mars, *J. Geophys. Res.*, *117*, E02009, doi:10.1029/2011JE003816.

Scholz, C. H., N. H. Dawers, J. Z. Yu, M. H. Anders, and P. A. Cowie (1993), Fault growth and fault scaling laws: Preliminary results, *J. Geophys. Res.*, *98*(B12), 21,951–21,961.

Schultz, R. A. (2003), Seismotectonics of the Amenthes Rupes thrust fault population, Mars, *Geophys. Res. Lett.*, *30*(6), 1303, doi:10.1029/2002GL016475.

Skinner, J. A. Jr., T. M. Hare, and K. L. Tanaka (2006), Digital renovation of the atlas of Mars 1:15,000,000-scale global geologic series maps, paper presented at 37th Annual Lunar and Planetary Science Conference, League City Texas, Lunar and Planetary Institute, Houston, TX, Abstract 2331.

Soderblom, L., C. Condit, R. West, B. Herman, and T. Kreidlera (1974), Martian planetwide crater distributions: Implications for geologic history and surface processes, *Icarus*, *33*(3), 239–263.

Teanby, N. A., and J. Wookey (2011), Seismic detection of meteorite impacts on Mars, *Phys. Earth Planet. Inter.*, *186*, 70–80.

Turcotte, D. L., R. Shcherbakov, B. D. Malamud, and A. B. Kucinskas (2002), Is the Martian crust also the Martian elastic lithosphere?, *J. Geophys. Res.*, *107*(E11), 5091, doi:10.1029/2001JE001594.

Vaucher, J., D. Baratoux, N. Mangold, P. Pinet, K. Kurita, and M. Grégoire (2009), The volcanic history of central Elysium Planitia: Implications for martian magmatism, *Icarus*, *204*(2), 418–442.

Vetterlein, J., and G. P. Roberts (2010), Structural evolution of the Northern Cerberus Fossae graben system, Elysium Planitia, Mars, *J. Struct. Geol.*, *32*, 394–406.

Werner, S. C., B. A. Ivanov, and G. Neukum (2009), Theoretical analysis of secondary cratering on Mars and an image-based study on the Cerberus Plains, *Icarus*, *200*, 406–417.

Wieczorek, M. A., and M. T. Zuber (2004), Thickness of the Martian crust: Improved constraints from geoid-to-topography ratios, *J. Geophys. Res.*, *109*, E01009, doi:10.1029/2003JE002153.